PHYSICAL REVIEW B **84**, 184112 (2011)

Mechanism for amorphization of boron carbide B_4C under uniaxial compression

Sitaram Aryal,[*] Paul Rulis, and W. Y. Ching
Department of Physics, University of Missouri–Kansas City, Kansas City, Missouri 64110, USA

(Received 25 July 2011; revised manuscript received 11 November 2011; published 28 November 2011)

Boron carbide undergoes an amorphization transition under high-velocity impacts, causing it to suffer a catastrophic loss in strength. The failure mechanism is not clear and this limits the ways to improve its resistance to impact. To help uncover the failure mechanism, we used *ab initio* methods to carry out large-scale uniaxial compression simulations on two polytypes of stoichiometric boron carbide (B_4C), $B_{11}C$-CBC, and B_{12}-CCC, where $B_{11}C$ or B_{12} is the 12-atom icosahedron and CBC or CCC is the three-atom chain. The simulations were performed on large supercells of 180 atoms. Our results indicate that the $B_{11}C$-CBC (B_{12}-CCC) polytype becomes amorphous at a uniaxial strain $s = 0.23$ (0.22) and with a maximum stress of 168 (151) GPa. In both cases, the amorphous state is the consequence of structural collapse associated with the bending of the three-atom chain. Careful analysis of the structures after amorphization shows that the $B_{11}C$ and B_{12} icosahedra are highly distorted but still identifiable. Calculations of the elastic coefficients (C_{ij}) at different uniaxial strains indicate that both polytypes may collapse under a much smaller shear strain (stress) than the uniaxial strain (stress). On the other hand, separate simulations of both models under hydrostatic compression up to a pressure of 180 GPa show no signs of amorphization, in agreement with experimental observation. The amorphized nature of both models is confirmed by detailed analysis of the evolution of the radial pair distribution function, total density of states, and distribution of effective charges on atoms. The electronic structure and bonding of the boron carbide structures before and after amorphization are calculated to further elucidate the mechanism of amorphization and to help form the proper rationalization of experimental observations.

DOI: 10.1103/PhysRevB.84.184112 PACS number(s): 61.50.Ks, 83.10.Tv, 81.05.Je, 82.40.Fp

I. INTRODUCTION

Boron carbide (B_4C) in its stoichiometric form is a hard, strong, and light-weight material[1] with a wide variety of applications. It is used, for example in body armor for soldiers, as a neutron-absorbent material, and for abrasive and wear-resistant parts. The stoichiometric boron carbide crystal has a space group of $R\bar{3}m$ (No. 166)[2] with 15 atoms in a rhombohedral primitive cell. It consists of a 12-atom icosahedron of B and a three-atom chain of C along the body diagonal, and it will be designated as B_{12}-CCC throughout this paper. By exchanging a C atom in the middle of the chain with a B atom at the polar site of the icosahedron, we arrive at the structure designated as $B_{11}C$-CBC. This is generally accepted as the most stable form of B_4C.[3,4] Figures 1(a) and 1(b) show the $B_{11}C$-CBC and B_{12}-CCC structures in the rhombohedral lattice with the B atoms in the middle of chain and the C atoms highlighted. In both polytypes, the icosahedron has six each of the so-called polar and equatorial sites. Each atom in the icosahedra has five nearest neighbor (NN) bonds within icosahedra. The polar atom has one extra bond with a polar atom in another icosahedron, and the equatorial atom has one short extra bond with a C atom at the end of the three-atom chain. The C atoms at the ends of the chains are fourfold bonded with three of the equatorial B atoms in different icosahedra and the central atom in the chain. Bond lengths (BLs) within chain atoms are relatively shorter, making the structure stiff along the chain direction.

With a very low density and high Hugoniot elastic limit (HEL) of about 22 GPa,[1,5,6] boron carbide is a very promising material for both personal and vehicle armor. However, boron carbide suffers from a sudden drop in its shear strength when the impact pressure is above the HEL.[5,7,8] Postfailure analysis of ballistic experiments indicates that boron carbide undergoes localized amorphization.[6] Amorphization of boron carbide was also observed under different types of nano-indentation[9–11] and under strong electric field.[12] The mechanism of B_4C amorphization under high-velocity impact is a subject of great theoretical and practical interest, but it is far from being fully understood, even with considerable experimental and theoretical efforts to understand it.

On the basis of data from low- and high-temperature Raman spectroscopy, Yan *et al.*[13] concluded that destruction of the three-atom chains leads to an amorphous structure composed of sp^2-bonded aromatic carbon rings and boron clusters with the $B_{11}C$ icosahedra remaining intact. On the other hand, Fanchini *et al.*,[14] on the basis of Gibb's free energy calculations, argued that B_{12}-CCC is the most likely polytype that can explain the amorphization of B_4C because the collapse of the B_{12}-CCC structure leads to the segregation of B_{12} icosahedra and carbon atoms to form a 2–3-nm-wide amorphous C band in excellent agreement with high-resolution electron microscopy images of samples recovered from ballistic impact experiments.[6] Fanchini *et al.* have also suggested the possible transformation of the $B_{11}C$-CBC structure into a B_{12}-CCC structure at high pressure, which can then lead to the amorphization of B_4C. Using Raman and photoluminescence spectroscopy along with Fourier transform infra-red analysis, Ghose *et al.*[11] concluded that dynamic indentation–induced amorphization of B_4C is due to the collapse of the $B_{11}C$-CBC unit cells to form amorphous B_{12} and C clusters. High pressure experiments using a diamond anvil cell found no pressure-induced amorphization in B_4C for pressures up to 507 GPa.[15,16] More recently, Yan *et al.*[17] reported the observation of localized amorphization of B_4C upon unloading from a high pressure state using *in situ* high-pressure Raman spectroscopy. They concluded that only nonhydrostatic stress can play a

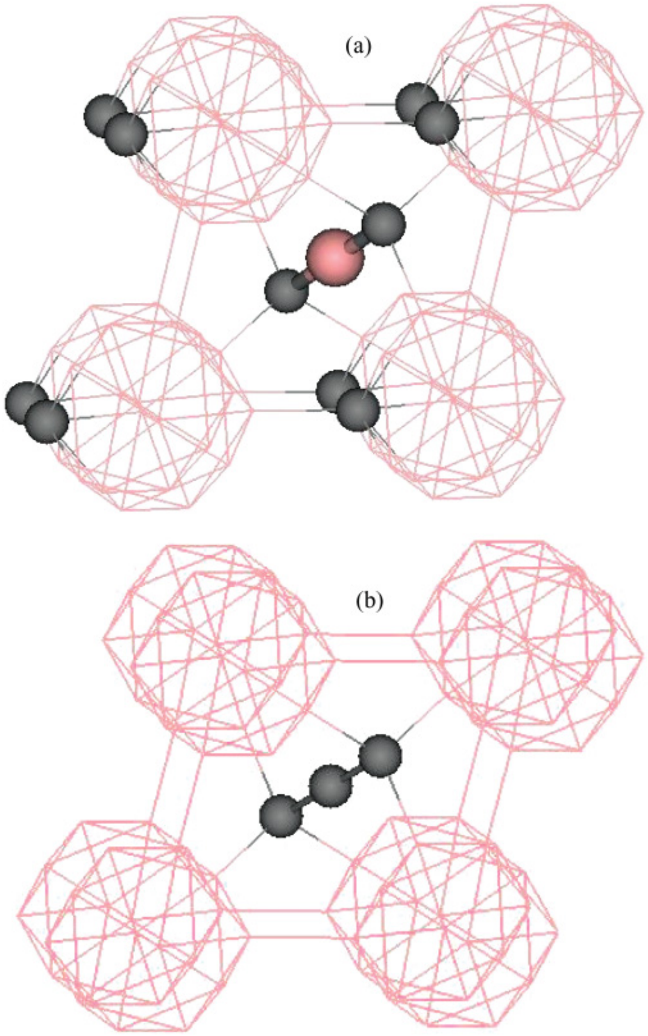

FIG. 1. (Color online) (a) $B_{11}C$-CBC and (b) B_{12}-CCC structure in the rhombohedral lattice. The small balls in the figures are C atoms, and the large ball in the middle of the C-B-C chain in image (a) is a B atom.

role in the localized amorphization. They have also performed first principles molecular dynamics simulations on a 15-atom rhombohedral unit cell of $B_{11}C$-CBC for both hydrostatic and uniaxial compressions along the axial direction. In the hydrostatic compression simulation up to 60 GPa, a smooth change in volume is observed. However, when compressed along the direction of the C-B-C chain, they found a 4% volume reduction for uniaxial pressure between 18.9 and 22.8 GPa. They related this sudden change in volume to the bending of the three-atom chain resulting in the amorphization of B_4C. In a shock wave compression experiment on a highly dense, pure B_4C polycrystalline sample, Zhang *et al.* determined the HEL of this sample to be 19.5 GPa and that a large change in the pressure density plot above 38 GPa signaled an onset of a phase transition.[18] However, the exact nature of this high-pressure phase was not elaborated.

From these previous efforts to understand the mechanism of amorphization in B_4C, it is obvious that an unambiguous picture does not emerge, and several key questions require clear answers: (1) Can hydrostatic compression lead to amorphization or is the uniaxial compression absolutely necessary? (2) Is the bending of the three-atom chain the key to amorphization? (3) Does amorphization of B_4C depend on whether the structure is $B_{11}C$-CBC or B_{12}-CCC? (4) Is it true that the $B_{11}C$-CBC structure reduces to B_{12} plus amorphous C upon amorphization? (5) How can the amorphous state of B_4C be unequivocally demonstrated? More importantly, none of the above works made a concerted effort to relate the structure of B_4C before and after amorphization to the fundamental electronic structure and bonding at the atomic level. To answer these questions and provide this relation, accurate large-scale simulations under well-controlled conditions in conjunction with atomic scale electronic structure and bonding calculation is necessary. In this paper, we report the results of such simulations using sufficiently large supercell models of $B_{11}C$-CBC and B_{12}-CCC for both hydrostatic and uniaxial compressions. In the next section, we briefly outline our methods and procedures used in the simulations. The results are presented and discussed in Sec. III. Section IV, is devoted to the summary and conclusions.

II. METHODS AND PROCEDURES OF SIMULATIONS

The rhombohedral unit cell of a crystal can be conveniently described using a hexagonal lattice with a cell size three times as large and the hexagonal c-axis aligned with the body diagonal of the original rhombohedral cell. Thus the hexagonal unit cell of B_4C contains 45 atoms with the three-atom chain aligned along the crystallographic c-axis. In the present study, we used a 2 × 2 × 1 hexagonal supercell with 180 atoms for both the $B_{11}C$-CBC and the B_{12}-CCC models. It must be emphasized that sufficiently large supercells are necessary for compression studies to ensure that the movements of the atoms in the crystal are not restricted by the periodic boundary of the unit cell, which could produce erroneous results. The structural data of the fully relaxed $B_{11}C$-CBC and B_{12}-CCC supercell models are presented in Table I. The $B_{11}C$-CBC model is quite distorted from perfect hexagonal symmetry. It has seven B (B1–B7) and three C (C1–C3) nonequivalent sites. B1, B2, B3, and B4 are equatorial B sites and B5, B6, and B7 are polar sites. B8 is in the middle of the chains between C1 and C2, whereas C3 is at the polar site of the icosahedron. The B_{12}-CCC model has only two B sites: the equatorial B (B1) and the polar B (B2). The C1 (C2) atoms are at the ends (middle) of the C-C-C chain. Table I also lists the nearest neighbor (NN) BLs for the nonequivalent atoms in both models. Figure 2 shows the sketch of the relaxed supercell model of $B_{11}C$-CBC and its projection on the a-b plane. These 180-atom supercell models are large enough to minimize the boundary effect in the total energy and stress-related simulations. It also provides flexibility for the formation of new or random bonding patterns because of structural changes under high strain.

For the computational part of our study, we used two well-established *ab initio* methods: the Vienna *ab initio* simulation package (VASP)[19–21] and the orthogonalized linear combination of atomic orbitals (OLCAO).[22] VASP is a plane wave–based method using pseudopotentials and is accurate for geometry optimization and total energy–related calculations. On the other hand, atomic orbitals are used as the basis set in the

TABLE I. Crystal structural data of $B_{11}C$-CBC and B_{12}-CCC supercell models.

Lattice Constants	$B_{11}C$-CBC	B_{12}-CCC
a, b	11.069, 11.087	
	11.162, 11.162	
c	11.907	11.961
α, β	90.00, 92.075	90.00, 90.00
γ	120.055	120.00
Nonequivalent sites and their bond lengths (Å). The integers in parentheses indicate the number of such bonds.		
B1	1.736, 1.742, 1.779	1.735 (2), 1.764 (2)
	1.771, 1.60, 1.738	1.770, 1.644
B2	1.732 (2), 1.775 (2)	1.701, 1.764 (2)
	1.782, 1.590	1.770, 1.807 (2)
B3	1.742 (2), 1.772 (2)	–
	1.569, 1.713	
B4	1.732, 1.736, 1.772	–
	1.789, 1.790, 1.596	
B5	1.725, 1.775, 1.779	–
	1.772, 1.779, 1.743	
B6	1.782, 1.813 (2)	–
	1.790 (2), 1.640	
B7	1.725, 1.772, 1.803	–
	1.771, 1.789, 1.813	
B8	1.418, 1.425	
C1	1.425, 1.600 (2), 1.590	1.644 (3), 1.321
C2	1.418, 1.596 (2), 1.569	1.321 (2)
C3	1.640, 1.714, 1.738 (2), 1.743 (2)	–

OLCAO method. It is very efficient and versatile for electronic structure and bonding calculations. The combination of the two methods has proved to be very effective in the study of physical properties of a large number of different materials with complex structures.[23–28]

In this work, VASP is used for structural relaxation of supercell models and for the evaluation of the stress tensor with total energy minimization at each step in the compression simulation. We used projector-augmented wave potentials[29,30] as supplied in the VASP package. To ensure high accuracy and in consideration of the large volume change during compression of the structure (and the expected sudden volume change at the phase change), a high cutoff energy of 700 eV, and a small electronic and ionic convergence criterion of 10^{-7} eV and 10^{-5} eV/Å, respectively, are adopted. Because the 180-atom supercell is fairly large, only the Γ-point is used in the k-point sampling. Next, we used the OLCAO method to investigate the electronic structure and local bonding of the compressed models by calculating the density of states (DOS), the distribution of effective charges, and their evolutions through the various strained structures. A full basis set consisting of 1s, 2s, 3s, 4s, 2p, 3p, 4p atomic orbitals of B and C was adopted.

Although the primary objective of this study is to investigate the behavior of the $B_{11}C$-CBC and B_{12}-CCC models under uniaxial compression, we have also performed a hydrostatic compression experiment to compare with the uniaxial compression results and to corroborate with experimental findings. Hydrostatic compressive strain is applied to both supercell models with a 1% volume decrease at each step, and the total energy and hydrostatic pressure are evaluated. For the uniaxial compression simulation, the structure is compressed along the chain direction (c-axis). At each step, the strain is increased by 1% and the structure is fully relaxed with the volume and the shape fixed. Then, the stress tensor and total energy values are extracted. There are two options for the compression simulation, one with constrained lattice vectors in the directions perpendicular to the compression, the other without constraints such that the lattice vectors are allowed to adjust in response to the compression. We chose the second option which is more realistic and closely mimic the ballistic impact experiments.

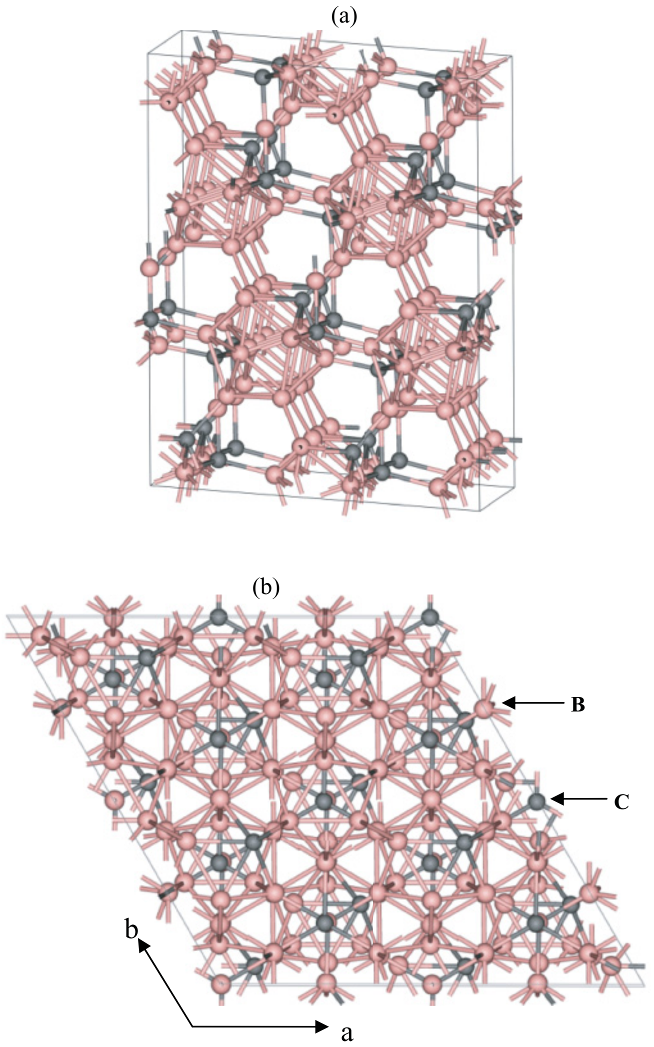

FIG. 2. (Color online) 180-atom supercell model of $B_{11}C$-CBC in the hexagonal lattice. (a) Slightly rotated about the c- and a-axes in a clockwise direction. (b) In crystallographic a-b plane. The larger balls are B atoms and smaller ones are C atoms.

III. RESULTS AND DISCUSSION

A. Results on hydrostatic compression

The results of hydrostatic compression on the $B_{11}C$-CBC and B_{12}-CCC models are displayed in Figures 3(a) and 3(b), respectively, where the hydrostatic pressure and total energy

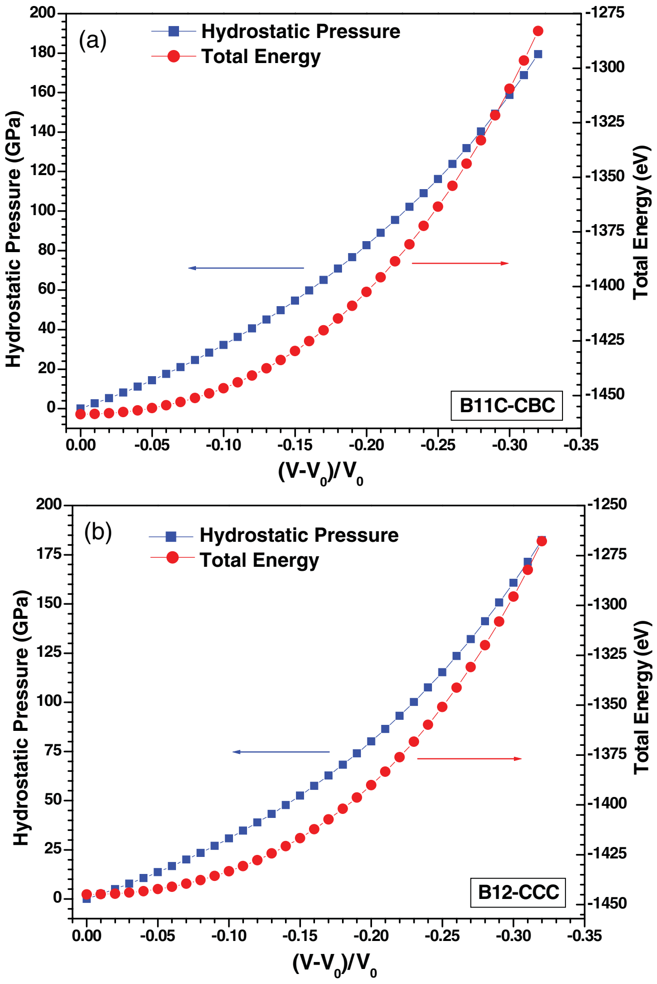

FIG. 3. (Color online) Hydrostatic pressure and total energy vs. hydrostatic strain $(V - V_0)/V_0$ in (a) B_{11}C-CBC model; (b) B_{12}-CCC model.

are plotted against the volume strain. Both structures were compressed hydrostatically up to 31% of their initial volume. The maximum hydrostatic pressure reached in this simulation is 179 GPa (182.5 GPa) for B_{11}C-CBC (B_{12}-CCC). As can be seen in Figure 3, the total energy varies smoothly in both models, indicating that there are no structural phase transitions involved. This is consistent with the experimental observation of Yan *et al.*[17] and seems to contradict the conclusion reached by Fanchini *et al.*[14] that B_{12}-CCC can transform to an amorphous state under a relatively smaller hydrostatic pressure of about 6 GPa.

B. Results on uniaxial compression

In contrast to the hydrostatic compression simulation, the results from uniaxial compressions are very different. The strain vs. stress plots for the B_{11}C-CBC and B_{12}-CCC models are shown in Figure 4. In the B_{11}C-CBC model, the stress increases almost linearly up to a strain of s = 0.23 and a corresponding stress of 168 GPa, indicating a near-perfect elastic deformation. This very high stress level before amorphization is a result of using a defect-free ideal crystal in the simulation and applying the compression along the chain direction. It is unlikely that such a high level can be reached in experiments using real material samples. After this point, there is a sudden and precipitous drop in stress to 20.9 GPa when the strain is increased to s = 0.24, signaling a drastic structural transformation. Beyond s = 0.24, the stress fluctuates up and down without any particular pattern, showing the absence of any residual elasticity in the structure.

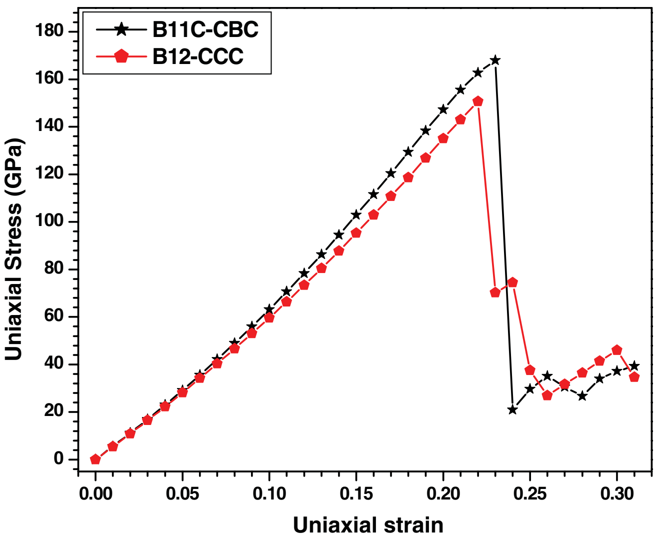

FIG. 4. (Color online) Uniaxial stress vs. uniaxial strain along the crystallographic c-axis in B_{11}C-CBC and B_{12}-CCC models.

In the B_{12}-CCC model, the deformation behavior under uniaxial compression is slightly different. Stress increases linearly up to a strain value of s = 0.22 with a corresponding maximum stress of 151 GPa. The sudden drop in stress from s = 0.22 to s = 0.23 suggests a drastic structural change. However, from s = 0.23 to 0.24, the stress actually rises slightly from 70.2 to 74.5 GPa. Thus, at these strain levels, the B_{12}-CCC model is not fully amorphized and still has some residual elasticity. On further compression, the stress ultimately drops to a minimum value of 26.9 GPa at s = 0.26, close to the minimum stress in the B_{11}C-CBC model. After amorphization and beyond s = 0.26, stress increases slightly and then it appears to fluctuate.

The above results strongly suggest that a drastic collapse in the structure has occurred and that this is associated with a phase transition from a crystalline state to the amorphous state. This will be verified by critical analysis of both the geometric structure and the electronic structure as presented below. It also shows that the B_{11}C-CBC model can withstand a uniaxial compressive stress slightly greater than the B_{12}-CCC model by 17 GPa and at a slightly higher strain. The residual strength observed in B_{12}-CCC is within a very narrow range of strain between s = 0.23 and 0.26. However, this issue might not play a significant role in what actually happens in ballistic impact experiments. In both models, our results clearly show that B_4C structures can resist a very high uniaxial stress along the chain direction. The maximum stress that the B_4C models can sustain under uniaxial compression is much larger than the reported HEL. However, in actual ballistic experiments or nano-indentation experiments, it is almost impossible to attain the ideal maximum compression condition as in the

TABLE II. Calculated elastic constants (C_{ij}) of the equilibrium structure of $B_{11}C$-CBC and B_{12}-CCC models (in GPa).

Crystal	C_{11}	C_{22}	C_{33}	C_{44}	C_{55}	C_{66}	C_{12}	C_{13}	C_{23}
$B_{11}C$-CBC	594.5	580.8	553.1	163.8	168.4	220.6	135.5	76.8	69.9
B_{12}-CCC	521.6	521.7	549.8	137.7	137.7	194.4	133.1	80.4	80.4
$B_{5.6}C$ (exp.) (Ref. 32)	542.8	542.8	534.5	164.8			130.6	63.5	

simulations. Yan *et al.*,[17] in their diamond cell experiment, reported the minimum pressure for amorphization of about 25 GPa. It is not clear whether the single crystal sample used in the experiments contains any defects or impurities that could significantly reduce the local elastic strengths. These defects may also divert the directional stress to shear stress, causing amorphization to occur at a smaller strain than that from ideal uniaxial compression along the chain direction. They have also performed a compressive molecular dynamics simulation along the C-B-C chain in the 15-atom $B_{11}C$-CBC model and concluded that there is an elastic deformation up to 18.9 GPa, followed by a sudden reduction in volume of about 4%. Their value of 18.9 GPa is almost a factor 10 less than the maximum stress in the present result and is likely affected by the limitation of the small cell they used.

C. Strain-dependent elastic coefficients

Elastic stiffness coefficients (C_{ij}) are the best representation of the elastic state and the mechanical strength of crystalline materials. When a material is compressed, its elastic state changes. The strain-stress curve discussed above only shows the linear elasticity along the direction of compression. On the other hand, C_{ij} values give not only the linear elasticity in other directions but also provide information on how a material may behave under shear stress. We have calculated the C_{ij} values of both $B_{11}C$-CBC and B_{12}-CCC supercell models at different uniaxial strains up to the maximum stress before the incipient amorphization using the strain-stress analysis scheme.[31] In this scheme, a small strain of −0.5% (compression) and +0.5% (stretching) is applied to the equilibrium structure for each independent strain element of the crystal. The deformed structure is optimized by using VASP; keeping the cell volume and shape fixed, the six components of the stress data (σ_i, $i =$ xx, yy, zz, yz, zx, xy) are calculated. The elastic tensor C_{ij} is obtained by solving the following equation:

$$\sigma_{ij} = \sum_{ij} C_{ij}\varepsilon_j \tag{1}$$

The calculated C_{ij} values for the unconstrained $B_{11}C$-CBC and B_{12}-CCC supercell models are presented in Table II. Overall, $B_{11}C$-CBC has considerably larger C_{ij} values than B_{12}-CCC. In $B_{11}C$-CBC, C_{11} and C_{22} are significantly different and larger than C_{33}. This difference arises from the presence of a C at the polar site and a B atom in the middle of chain that breaks the symmetry. In B_{12}-CCC, C_{11} and C_{22} are equal and smaller than C_{33}. Table II also lists the measured C_{ij} values[32] of a carbon-deficient single crystal sample of $B_{5.6}C$ at room temperature. The agreement with our calculated values for the stoichiometric model is reasonable. The measured C_{11} and C_{22} values are between those of $B_{11}C$-CBC and B_{12}-CCC, whereas the measured C_{33} is smaller than the calculated C_{33} in both models.

Figure 5 shows the calculated C_{ij} values of the $B_{11}C$-CBC and B_{12}-CCC supercell models at different uniaxial strains. As the uniaxial strain increases, C_{11}, C_{22}, and C_{33} all increase, but the increase in C_{33} is much faster than others because the strain is along the crystallographic c-axis. When the uniaxial strain reaches 0.20, they start to decrease quite rapidly. On the other hand, the shear elastic constants C_{44}, and C_{55} remain fairly constant up to the uniaxial strain of $s = 0.15$. Beyond strain 0.15, these shear elastic constants start to decrease. The shear elastic constant C_{66} is almost constant up to the failure point in both polytypes. This result shows the complicated effect of uniaxial compression on the elastic coefficients in B_4C polytypes. Reduced C_{44} and C_{55} values may lead to the failure of the structure at a strain smaller than that indicated in Figure 4. Furthermore, it also shows that both B_4C polytypes are less resistant to shear strain (stress). It is conceivable that both structures may undergo transformation at a smaller

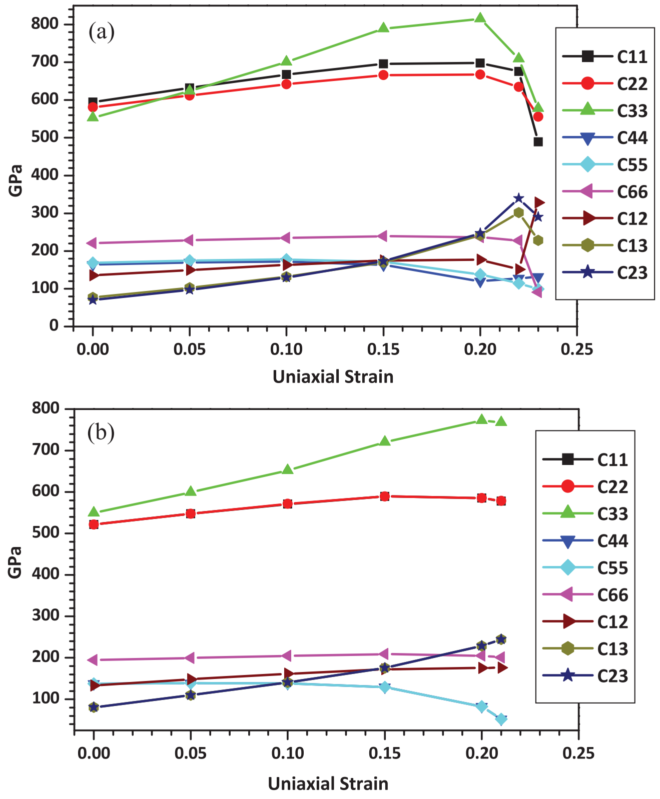

FIG. 5. (Color online) Calculated C_{ij} values at different uniaxial strains along the crystallographic c-axis in (a) $B_{11}C$-CBC and (b) B_{12}-CCC.

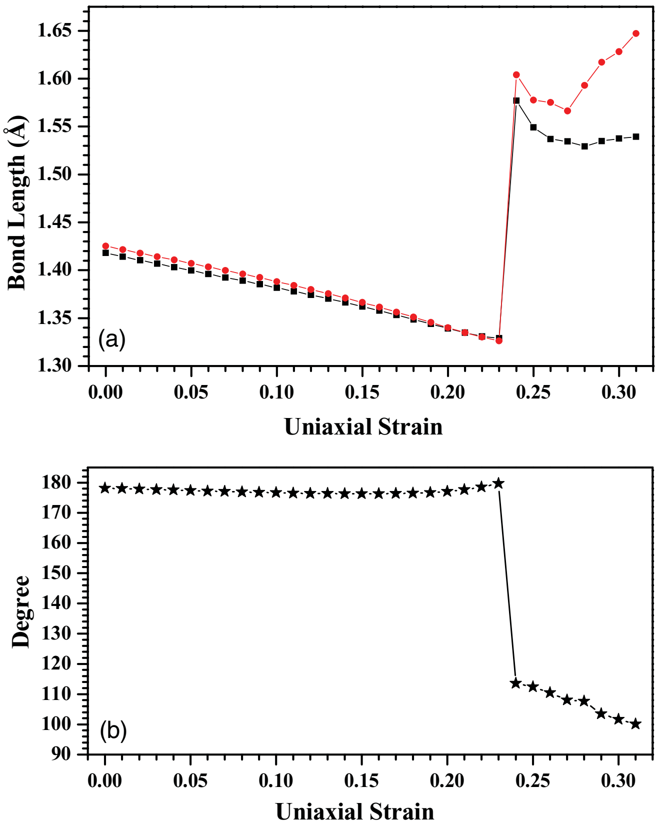

FIG. 6. (Color online) Plots of (a) average bond lengths and (b) average chain angle vs. uniaxial strain (ε) along the crystallographic c-axis in the $B_{11}C$-CBC model.

uniaxial strain depending on stoichiometry and other factors related to the nature of the sample.

D. Structural analysis of supercell models under uniaxial strain

We now analyze structural changes in $B_{11}B$-CBC and B_{12}-CCC models under uniaxial compression. The B atom in the middle of the chain in the $B_{11}C$-CBC model has two unequal B-C bonds because of the presence of the C atom at the polar site of the icosahedra. The evolution of these two B-C bonds as a function of uniaxial strain is plotted in Figure 6(a). As the compression increases, both bonds decrease uniformly and become equal at strain 0.23. Beyond strain 0.23, where drastic structural change occurs, their BLs increase suddenly

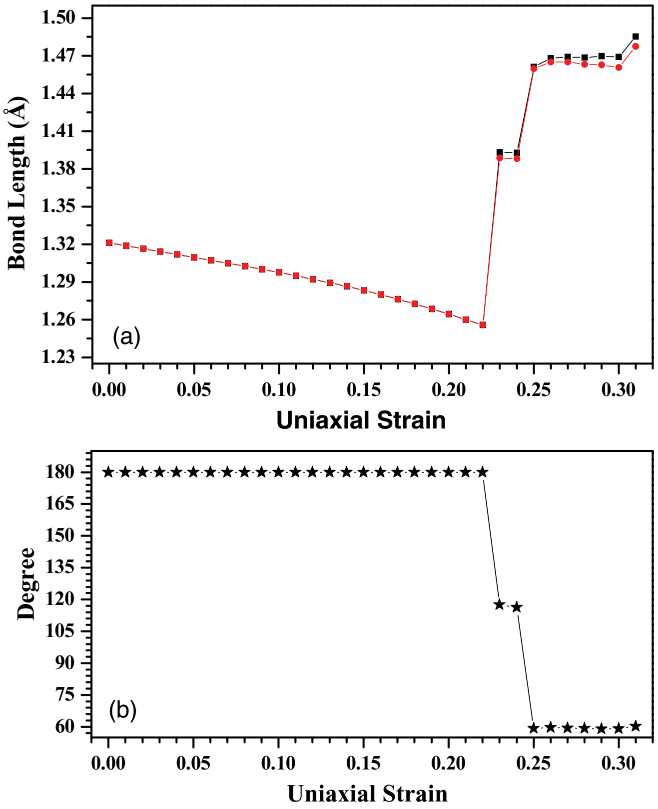

FIG. 8. (Color online) Plots of (a) average bond lengths and (b) average chain angle vs. uniaxial strain (ε) along the crystallographic c-axis in B_{12}-CCC model.

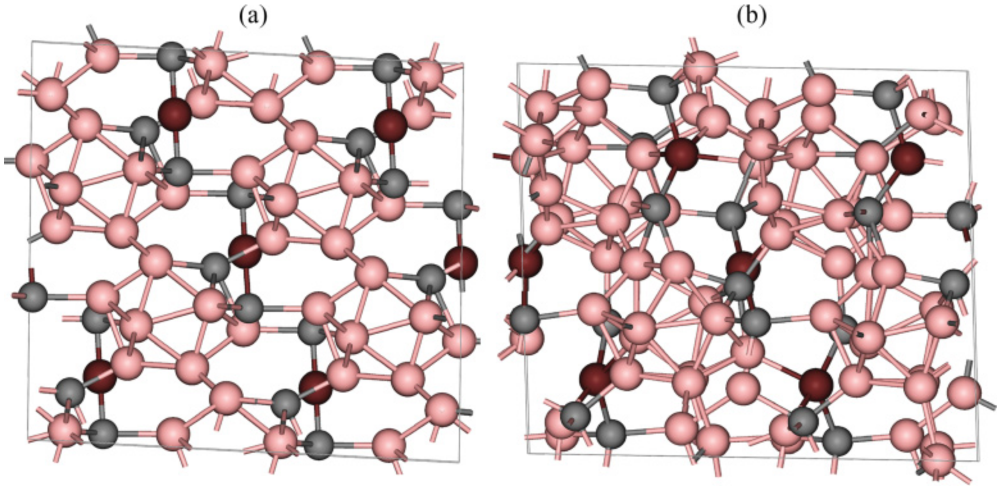

FIG. 7. (Color online) Atomic configurations in $B_{11}C$-CBC model at different uniaxial strains. B atoms in the middle of chains are colored differently for easy visual distinction. (a) At strain 0.23; (b) at strain 0.24. (Pink [light gray] = B in icosahedra; grey [medium gray] = C; dark violet [dark gray] = B in chain)

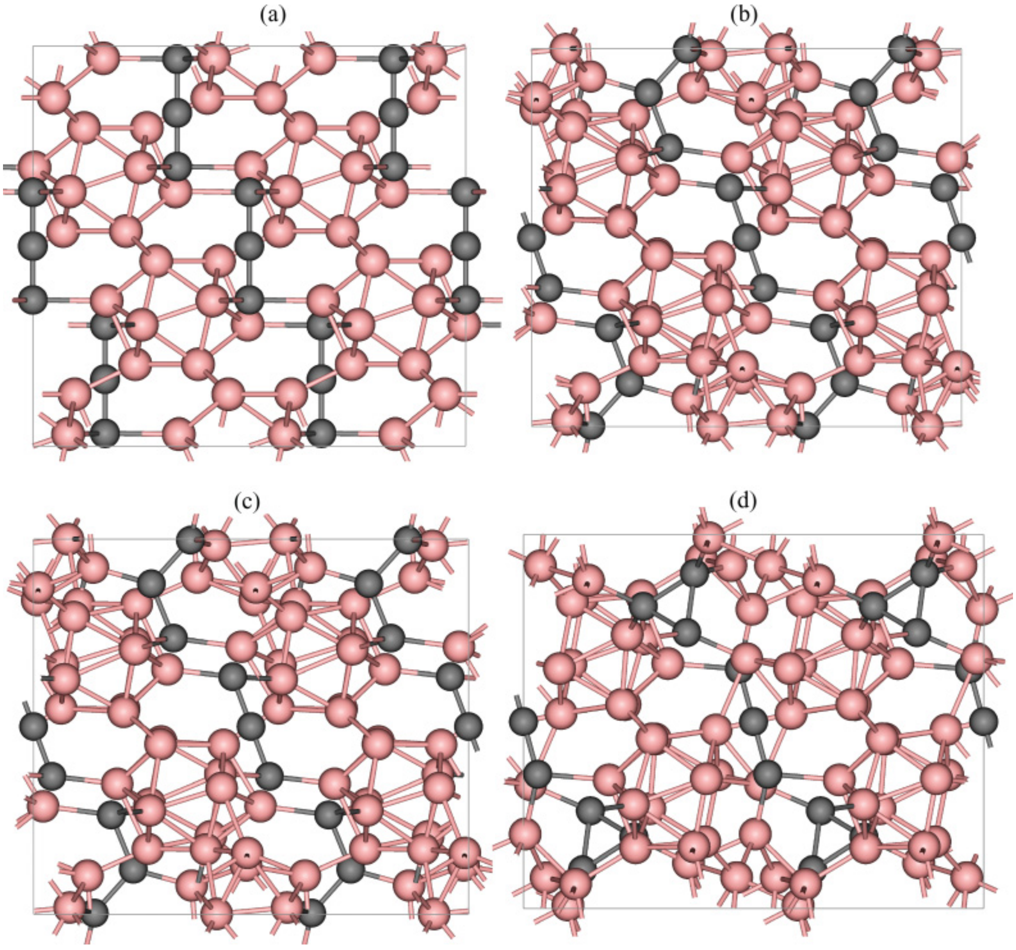

FIG. 9. (Color online) Atomic configurations in B_{12}-CCC model at different uniaxial strains. (a) At s = 0.22, (b) at s = 0.23, (c) at s = 0.24, and (d) at s = 0.25. (Pink [light gray] = B; grey [medium gray] = C)

and large differences emerge. Figure 6(b) shows the change in the average C-B-C chain angle with uniaxial strain. The average chain angle is almost constant (close to 180°) up to s = 0.23 and then a sudden decrease associated with the bending of the chain takes place. Figures 7(a) and 7(b) displays snapshots of B_{11}C-CBC at uniaxial strains of 0.23 and 0.24, respectively. As can be seen, at s = 0.23 the C-B-C chains are almost straight along the crystallographic c-axis, and the B_{11}C icosahedra are intact. But at s = 0.24, the chains are no longer straight and they bend at different angles, ranging from 105.7° to 121.7°. The B atoms in the middle of the chain now make one, two, or three extra bonds with other B atoms in different deformed icosahedra. The model at s = 0.24 has a slightly larger lattice constant b than a, and the hexagonal structure no longer holds. The B_{11}C icosahedra are highly deformed but not totally broken, suggesting that the bending of the three-atom chains is the main source of amorphization under uniaxial compression. This is in agreement with the conclusion of Ref. 17.

In the B_{12}-CCC model, the C-C bonds in the thee-atom chain are identical. Figure 8(a) shows the averages of the C-C bonds as a function of strain, which decreases uniformly up to the strain of 0.22. Beyond s = 0.22, the C-C BLs suddenly increase and are no longer identical. Figure 8(b) shows the change in the average C-C-C chain angle under uniaxial compression. They are perfectly straight until the strain reaches 0.22. Beyond s = 0.22, at s = 0.23 and s = 0.24, some of the chains start to bend. At s = 0.25 and beyond in the amorphous region, the average angle is about 60°, indicating the formation of triangular carbon units. Figure 9 shows the snapshots of the B_{12}-CCC model at the strains of 0.22–0.25. The C-C-C chains are perfectly straight along the c-axis at s = 0.22 and the B_{12} icosahedra are somewhat undistorted. At s = 0.23 and 0.24, some of the chains are still straight, but inclined from the axial direction, and the rest are bent. The average chain angle of the bent C-C-C chains at strains 0.23 and 0.24 are 117.6° and 116.3°, which are close to the average angle of the bent C-B-C chains in the B_{11}C-CBC model at s = 0.24. This implies that the intermediate residual elastic strength in B_{12}-CCC at strains between 0.22 and 0.24 occurs because some of the chains tend to incline instead of bend. When the C-C-C chain bends, the middle C atom makes one extra bond with a B atom in the B_{12} icosahedron. When the C-C-C chain inclines, it loses one C-B bond to an icosahedron. In this process of breaking and forming new bonds, B_{12} icosahedra are distorted and the structure undergoes an irreversible change. At strain 0.25, the bent C-C-C chains form near perfect triangles with each C atom making two

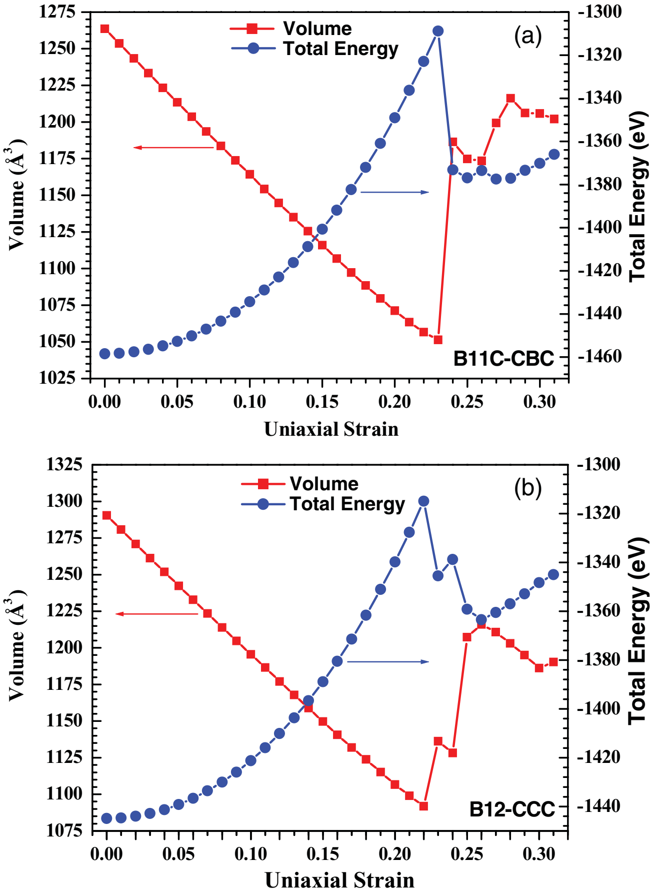

FIG. 10. (Color online) Change in volume and total energy with uniaxial strain along the crystallographic c-axis in: (a) $B_{11}C$-CBC model; (b) B_{12}-CCC model.

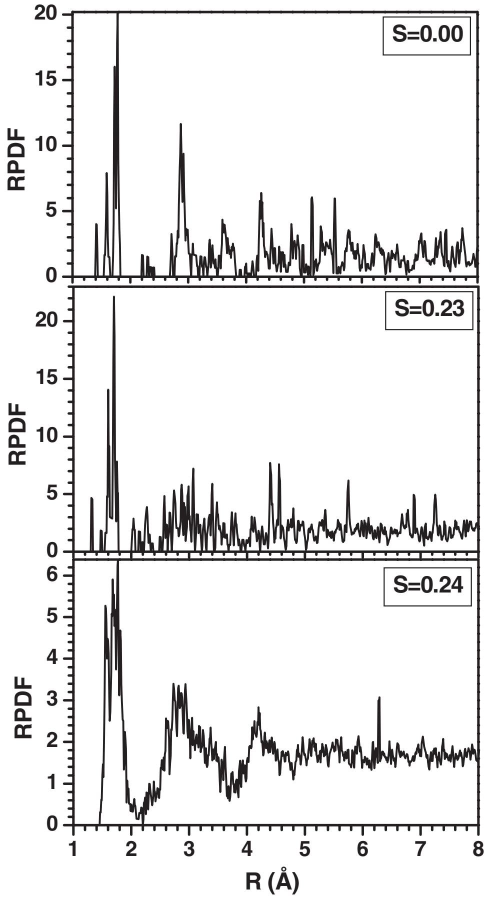

FIG. 11. RPDF plots of $B_{11}C$-CBC model at different uniaxial strains (s) along the crystallographic c-axis.

other C-B bonds. In this amorphous region, the icosahedra are severely deformed with some intra-icosahedral B-B bonds being broken.

A structural phase transition is always accompanied by a large change in total energy and volume. Figures 10(a) and 10(b) shows the total energy and volume changes with uniaxial compression. In both cases, total energy increases smoothly and the volume decreases linearly until they reach their respective strains needed for amorphization. In $B_{11}C$-CBC, there is a 12.8% volume increase and a 4.8% total energy decease between s = 0.23 and s = 0.24. These changes in volume and total energy are rather large, a manifestation of fundamental structural variation. Similarly, in B_{12}-CCC, there is a 4% volume increase and a 2.3% total energy decrease from s = 0.22 to s = 0.23 and a further 10.6% volume increase and a 3.4% total energy decrease from s = 0.22 to s = 0.25. It is generally expected that a sudden drop in the elasticity of the structure should result in an expansion in the unconstrained directions.

E. Evidence of amorphization: Radial pair distribution function

It is clear from the results shown above that both $B_{11}C$-CBC and B_{12}-CCC structures of B_4C suffer catastrophic structural changes beyond the uniaxial strains of 0.23 and 0.22, respectively. So the question arises: Is there additional clear and unequivocal evidence for the formation of an amorphous structure? A traditional way to distinguish the crystalline and amorphous structures is to calculate their radial pair distribution function (RPDF). Figure 11 shows the RPDF plots of the $B_{11}C$-CBC model at uniaxial strains of 0.00, 0.23, and 0.24. At s = 0.00 the structure is unstrained, so the RPDF is that of a perfect B_4C crystal with well-defined peaks corresponding to different B-C, B-B, and C-C separations. At the high strain of s = 0.23, these structures in the RPDF are clearly visible, showing that the long-range order associated with the crystallinity of the structure has persisted. The compression resulted only in a slight broadening of the peaks. However, at s = 0.24, the distinctive sharp peaks all disappear and the resulting RPDF has highly broadened peaks characteristic of an amorphous solid.

Similar trends can be observed in the RPDF plots of the B_{12}-CCC model. The RPDF plots of B_{12}-CCC at strains of 0.00, 0.22, and 0.23 are shown in Figure 12. At strains 0.00 and 0.22, the RPDF plots have well-defined peak features displaying long-range order in the structure. At strain 0.23, the long-range order disappears. Unlike in B_{11}-CBC, the B_{12}-CCC model shows some short-range order, even after amorphization from the formation of triangular C units discussed above.

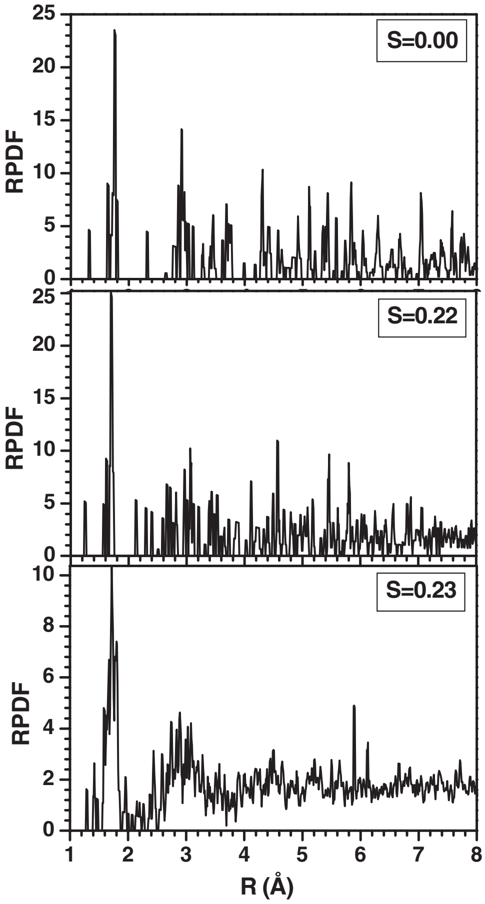

FIG. 12. RPDF plots of B_{12}-CCC model at different uniaxial strains (s) along the crystallographic c-axis.

F. Evidence of amorphization: Electronic structure and bonding

Another very effective way to investigate amorphization in B_4C is to calculate quantum mechanically the effective charge (Q^*) on each atom in the model using the OLCAO method with a minimal basis set. Q^* is the valence electronic charge associated with a particular atom α in the crystal calculated according to the Mullikan scheme:[33]

$$Q^*_\alpha = \sum_i \sum_{n.\mathrm{occ}} \sum_{j,b} C^{*n}_{i\alpha} C^n_{j\beta} S_{i\alpha,j\beta}. \tag{2}$$

In Eq. (2), $C^n_{j\beta}$ are the eigenvector coefficients of the nth band, jth orbital, and βth atom, and $S_{i\alpha,j\beta}$ are the overlap integrals between the ith orbital of the αth atom and jth orbital of the βth atom. The deviation of Q^* from the charge of the neutral atom shows the gain or loss of charge as a consequence of interatomic interaction and provides important information about the structure at the atomistic level. Figure 13 shows the effective charge distribution of the 180 B and C atoms in B_{11}C-CBC model at different strains of s = 0.00, 0.23, and 0.24. Atoms numbered 1–72 are the equatorial B atoms; atoms numbered 73–132 are polar B atoms; atoms 133–144 are the B atoms in the middle of the chain; atoms 145–168 are C atoms in the chain, and those from 169–180 are the C atoms at the polar sites of the icosahedra. Horizontal lines at 3 and 4 represent the electron charge of the neutral B and C atoms to facilitate identifying charge gain or loss. On average, B atoms lose charge to C atoms. At strain 0.00, the Q^* distribution shows four groups for equatorial B and three groups for polar B. These subgroups within the equatorial or polar sites in the icosahedra occur because of the presence of a C atom in one of the polar sites, which breaks the icosahedral symmetry. The process of gaining or losing charge by B atoms in B_{11}C icosahedra appears to be quite complicated. The B atoms in the middle of the chain, which have short B-C bonds, lose a relatively large amount of charge. Among the C atoms, the polar C atoms, which have longer bonds, gain a smaller amount of charge. At a strain of 0.23 before amorphization, differences in Q^* among the B atoms within the icosahedra have widened because of increased influence of the polar C atoms. An unusual feature at s = 0.23 is that the atoms numbered 61–84, which originate from polar and equatorial B atoms, have almost equal Q^*. This reflects a decrease in the distinction between equatorial and polar sites at higher strains. At a strain of 0.23, the B atoms in the middle of the chains have gained a significant amount of charge but still retain their own identity. Furthermore, the difference in Q^* of the chain C atoms is diminished, which is consistent with the observation in the average BL plots (Figure 6). The most conspicuous feature of the effective charge distribution is at strain 0.24. The Q^* of B atoms are widely scattered, showing no trace of any group identity. Similarly, polar C and chain C atoms have lost their distinction. All the atoms in the structure have different and widely distributed values of Q^*, an unequivocal signature of amorphization.

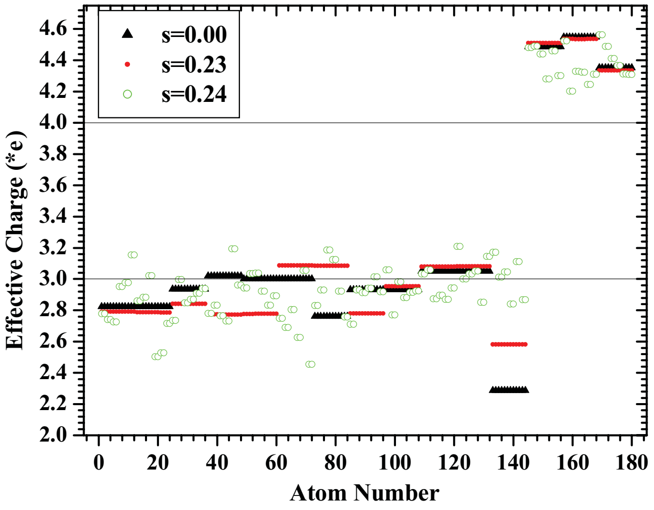

FIG. 13. (Color online) Distribution of effective charge Q^* at uniaxial strains (s) of 0.00, 0.23, and 0.24 in B_{11}C-CBC model. Horizontal lines at 3.0 and 4.0 represent the number of valence electrons in neutral B and C atoms, respectively.

Similar analysis of the effective charge distribution in the B_{12}-CCC supercell model at different strains is presented in Figure 14. The atoms are labeled as follows: equatorial B atoms (0–72), polar B atoms (73–144), and C atoms at the ends of the chain (145–168) and at the center of the chain (169–180). At s = 0.00, all Q^* values are distinct and well separated. Equatorial B atoms have lost some of their charge, whereas polar B atoms have gained slightly. The C atoms at the middle of the C-C-C chains, which have short bonds with other C

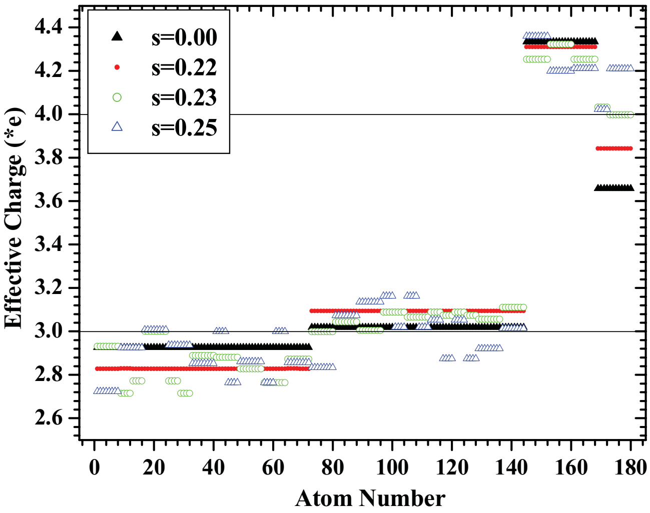

FIG. 14. (Color online) Distribution of effective charge Q^* at uniaxial strains (s) of 0.00, 0.22, 0.23, and 0.25 in B_{12}-CCC model. Horizontal lines at 3.0 and 4.0 represent the number of valence electrons in neutral B and C atoms, respectively.

atoms, have lost charge significantly. On the other hand, the C atoms at the ends of chain, which have relatively short bonds with equatorial B atoms, gain a larger amount of charge. At strain $s = 0.22$, the difference in Q^* between equatorial and polar B widens, but they still maintain their own identity. At strains 0.23 and 0.25 all long-range order in the structure is lost, and one would expect the Q^* distribution to be widely scattered as in the B_{11}C-CBC model. However, the calculated Q^* distribution shows that the B_{12}-CCC model still maintains some kind of short-range order. This is consistent with the RPDF plots shown in Figure 12.

To further confirm the amorphization of B_4C under uniaxial compression and to observe the evolution of electronic structure, we have calculated the total density of states (TDOS) of both B_{11}C-CBC and B_{12}-CCC models at different strains using the OLCAO method with a full-basis set. The results are displayed in Figures 15 and 16. The TDOS can be resolved into partial components of different atomic and orbital origins (not shown here). These two models have quite different TDOS features. B_{12}-CCC has a strong peak in the middle of the band gap originating from the 2p orbitals of C atoms in the middle of chain. In both models, the upper part of the valance band (VB) is dominated by B atoms and lower part by C atoms. In the conduction band (CB) region, the TDOS features are mostly dominated by B atoms. B_{11}C-CBC and B_{12}-CCC both have indirect band gaps. (The calculated band structures are not presented here.) At strain 0.00, B_{11}C-CBC has a band gap of 2.76 eV, which is significantly smaller than that found for B_{12}-CCC, which is 4.06 eV if the strong peak is considered to be in the middle of the gap. If the gap states are considered to be part of the unoccupied CB, a direct band gap of 1.26 eV is obtained. Previously, Li and Ching[34] calculated band structure of the B_{11}-CBC model using an older version of the OLCAO method and reported an indirect band gap 3.03 eV. The difference is attributed to the slightly better basis set used and a more accurate potential representation in the present calculation. Also, the structure of the present

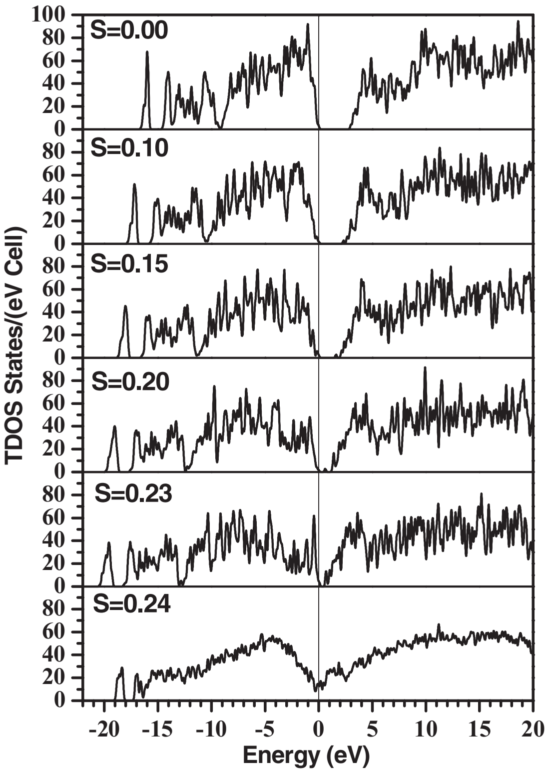

FIG. 15. Calculated total density of states (TDOS) of B_{11}C-CBC model at different strains (s). Vertical line represents top of the VB, which is set to 0 eV.

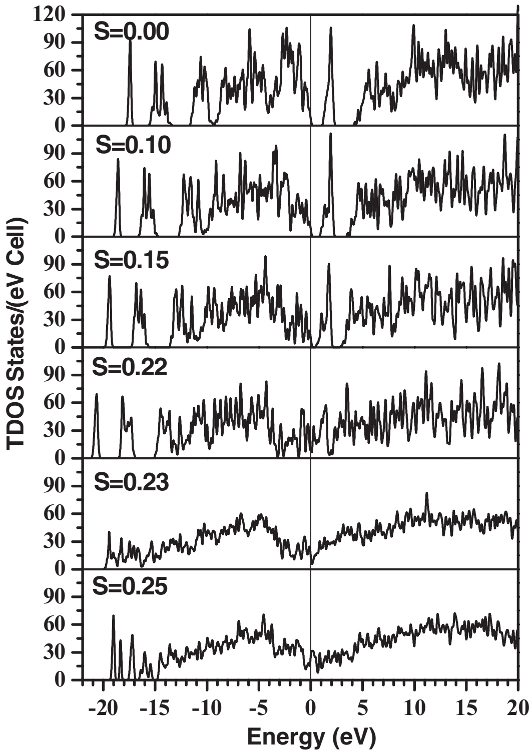

FIG. 16. Calculated total density of states (TDOS) of B_{12}-CCC model at different strains (s). Vertical line represents top of the VB, which is set to 0 eV.

$B_{11}C$-CBC supercell model is a fully relaxed model instead of the experimental structure. Plenty of calculations[35,36] report band gaps of $B_{11}C$-CBC or B_{12}-CCC polytypes, but most of them are larger than the recently reported band gap value of about 2.1 eV.[37,38] On the other hand, the direct band gap of 1.56 eV presented by Dekura *et al.*,[39] taken from the top of the VB to the bottom of the mid-gap DOS feature, is slightly larger than our value of 1.26 eV. It should be pointed out that any measured gap value for B_4C has a large degree of uncertainty because of the defective nature and nonstoichiometric composition of the sample.

Figures 15 and 16 show that as compression increases, the band gap decreases and the upper VB broadens. The band gap values of $B_{11}C$-CBC at strains of 0.10, 0.15, 0.20, and 0.23 are 2.30, 1.95, 1.20, and 0.55 eV, respectively. At a strain of $s = 0.24$, the band gap completely disappears, and the DOS shows the features typical of an amorphous solid. The pattern of evolution of the TDOS in the B_{12}-CCC model is similar to that of $B_{11}C$-CBC. Band gaps for B_{12}-CCC at strains of 0.10 and 0.15 are 3.48 and 2.82 eV, respectively. At a strain $s = 0.22$, the band gap almost disappears, but the TDOS still shows crystalline features. Beyond the strain of 0.22, the TDOS features are quite broadened and clearly show the amorphous nature of the structure.

IV. SUMMARY AND CONCLUSIONS

We have performed compression simulations using *ab initio* techniques on large supercell models of B_4C ($B_{11}C$-CBC and B_{12}-CCC) for both hydrostatic and uniaxial compressions. Under hydrostatic compression, smooth changes in pressure and total energy were observed up to a very high strain of 0.32, with no sign of abrupt structural change to an amorphous state. On the other hand, when compressed along the uniaxial chain direction, the structure undergoes a massive structural change to an amorphous state at a uniaxial strain of 0.23 (0.22) for the $B_{11}C$-CBC (B_{12}-CCC) model. The change in total energy and volume at the point of amorphization is large and discontinuous, so it can be classified as a first-order phase transition. The maximum stress that the $B_{11}C$-CBC (B_{12}-CCC) model can withstand is 168 GPa (152 GPa). The B_{12}-CCC model shows some residual strength at strains 0.23 and 0.24. The amorphization of the B_4C crystal is further confirmed by detailed analysis of the evolution of the RPDF and TDOS and of the distribution of effective charges in both models. In both cases and just before amorphization, the icosahedra remain intact and all the three-atom chains are straight along the c-axis. After amorphization, the icosahedra are still identifiable but severely distorted because of the formation of new bonds with the compressed chain atoms. These results clearly indicate that the bending of the three-atom chain is the main starting event that leads to amorphization. Amorphization in the two B_4C models shows some discernable differences. Amorphization in the $B_{11}C$-CBC model is abrupt, and no short-range order remains, whereas in the B_{12}-CCC model, it appears that some short-range order remain even after amorphization, mostly in the formation of local triangular C units. This fact could partially rationalize the notion of aggregation of some short-range structures of B and C atoms in amorphized B_4C, as suggested by Fanchini *et al.*[14]

Our large-scale *ab initio* simulations provide detailed information on amorphization at the atomic scale that was missing in most previous studies. We have revealed the subtle differences in the amorphization process depending on whether the B_4C structure is $B_{11}C$-CBC or B_{12}-CCC. In real samples, the presence of both polytypes is probable. Our calculated maximum stress that B_4C can withstand is much larger than those reported from ballistic experiments. This is because our uniaxial compression simulation is strictly along the direction of the chain, which sets the upper limit for the maximum stress. If the B_4C structures are compressed in other crystallographic directions, different failure points are expected owing to the anisotropic crystal structure. On the other hand, the calculated C_{ij} at different strains in both models show that the structure is significantly weaker in resisting shear strains. The B_4C structure may collapse under a shearing stress that is much less than uniaxial stress.

The real B_4C materials used for armor protection and subject to ballistic impact tests are either polycrystals or composites. The processed samples are usually nonstoichiometric and polycrystalline, and the presence of impurities, defects, and microstructures such as grain boundaries or dislocations is the norm. The failure mechanism in the real samples will be far more complex. Many other factors in actual experiments, such as impact contact area, impact duration, impact velocity, impact orientation, and other unaccounted factors in the actual ballistic experiments, might cause the shear stress to reach a sufficiently high level that could result in localized amorphization within certain regions, as observed experimentally. Our simulation on the idealized models provides the necessary insights in understanding such failure and set the upper limits for the failure strain. It is desirable to conduct the same uniaxial compression simulation with even larger supercells of more than 180 atoms, which can reduce the constraints imposed by the periodic boundary condition and more closely approach the characteristic length scale of the amorphous material. Similar simulations on much larger models containing different kinds of imperfections or on composites materials with other ceramics such as SiC can be used to help identify promising ingredients and processing conditions for the production of armor materials with superior properties.

ACKNOWLEDGMENTS

This work was supported by the US Department of Energy under grant No. DE-FG02-84DR45170 and partially by DOE-NETL under Grant No. DE-FE0004007. This research used the resources of NERSC supported by the Office of Basic Science of DOE under Contract No. DE-AC03-76SF00098.

---

*sra3zd@mail.umkc.edu

[1] F. Thevenot, J. Eur. Ceram. Soc. **6**, 205 (1990).

[2] D. Emin, T. Aselage, A. C. Switendick, B. Morosin, and C. L. Beckel, *AIP Conference Proceedings 231. Boron-rich Solids. Albuquerque*, *New Mexico 1990*, p. 195.

[3] R. Lazzari, N. Vast, J. M. Besson, S. Baroni, and A. Dal Corso, Phys. Rev. Lett. **83**, 3230 (1999).

[4] J. E. Saal, S. Shang, and Z.-K. Liu, Appl. Phys. Lett. **91**, 231915 (2007).

[5] D. E. Grady, *Dynamic Properties of Ceramic Materials: Sandia National Laboratories Report*, SAND 94-3266 (Sandia National Laboratories, Albuquerque, NM, 1995).

[6] M. W. Chen, J. W. McCauley, and K. J. Hemker, Science **299**, 1563 (2003).

[7] D. P. Dandekar, *Army Research Laboratory*, ARL-TR-2456 (Aberdeen Proving Ground, Aberdeen, MD, 2001).

[8] T. J. Vogler, W. D. Reinhart, and L. C. Chhabildas, J. Appl. Phys. **95**, 4173 (2004).

[9] V. Domnich, Y. Gogotsi, M. Trenary, and T. Tanaka, Appl. Phys. Lett. **81**, 3783 (2002).

[10] D. Ge, V. Domnich, T. Juliano, E. A. Stach, and Y. Gogotsi, Acta Mater. **52**, 3921 (2004).

[11] D. Ghose, G. Subhash, C. H. Lee, and Y. K. Yap, Appl. Phys. Lett. **91**, 061910 (2007).

[12] G. Fanchini, V. Gupta, A. B. Mann, and M. Chhowalla, J. Am. Ceram. Soc. **91**, 2666 (2008).

[13] X. Q. Yan, W. J. Li, T. Goto, and M. W. Chen, Appl. Phys. Lett. **88**, 131905 (2006).

[14] G. Fanchini, J. W. McCauley, and M. Chhowalla, Phys. Rev. Lett. **97**, 035502 (2006).

[15] R. J. Nelmes, J. S. Loveday, R. M. Wilson, W. G. Marshall, J. M. Besson, S. Klotz, G. Hamel, T. L. Aselage, and S. Hull, Phys. Rev. Lett. **74**, 2268 (1995).

[16] T. J. Holmquist and G. R. Johnson, J. Appl. Phys. **100**, 093525 (2006).

[17] X. Q. Yan, Z. Tang, L. Zhang, J. J. Guo, C. Q. Jin, Y. Zhang, T. Goto, J. W. McCauley, and M. W. Chen, Phys. Rev. Lett. **102**, 075505 (2009).

[18] Y. Zhang *et al.*, J. Appl. Phys. **100**,113536 (2006).

[19] G. Kresse and J. Hafner, Phys. Rev. B **47**, 558 (1993).

[20] G. Kresse and J. Furthmüller, Comput. Mater. Sci. **6**, 15 (1996).

[21] G. Kresse and J. Furthmüller, Phys. Rev. B **54**, 11169 (1996).

[22] W. Y. Ching, J. Am. Ceram. Soc. **73**, 3135 (1990).

[23] P. Rulis, H. Yao, L. Ouyang, and W. Y. Ching, Phys. Rev. B **76**, 245410 (2007).

[24] W. Y. Ching, L. Ouyang, P. Rulis, and H. Yao, Phys. Rev. B Condens. Matter Mater. Phys. **78**, 014106 (2008).

[25] J. Chen, L. Ouyang, P. Rulis, A. Misra, and W. Y. Ching, Phys Rev Lett **95**, 256103 (2005).

[26] W. Y. Ching, Paul Rulis, L. Ouyang, S. Aryal, and A. Misra, Phys. Rev. B **81**, 214120 (2010).

[27] Lei Liang, Paul Rulis, and W. Y. Ching, Acta Biomaterialia **6**, 3763 (2010).

[28] Lei Liang, Paul Rulis, L. Ouyang, and W. Y. Ching, Phys. Rev. B **83**, 024201 (2011).

[29] P. E. Blöchl, Phys. Rev. B **50**, 17953 (1994).

[30] G. Kresse and D. Joubert, Phys. Rev. B **59**, 1758 (1999).

[31] O. H. Nielsen and R. M. Martin, Phys. Rev. Lett. **50**, 697 (1983).

[32] K. J. Mcclellan, F. Chu, J. M. Roper, and I. Shindo, J. Mater. Sci. **36**, 3403 (2001).

[33] R. S. Mullikan, J. Chem. Phys. **23**, 1833 (1955). **23**, 1841 (1955).

[34] D. Li and W. Y. Ching, Phys. Rev. B **52**, 17073 (1995).

[35] D. M. Bylander, L. Kleinman, and S. Lee, Phys. Rev. B **42**, 1394 (1990).

[36] D. W. Bullett, J. Phys. C **15**, 415 (1982).

[37] H. Werheit, M. Laux, U. Kuhlmann, and R. Telle, Phys. Status Solidi B **172**, K81 (1992).

[38] H. Werheit, H. W. Rotter, S. Shalamberidze, A. Leith-Jasper, and T. Tanaka, Phys. Status Solidi B **248**, 1275 (2011).

[39] H. Dekura, K. Shirai, and A. Yanase, J. Phys. Conf. Ser. **215**, 012117 (2010).